scientific reports

OPEN

# Regiomontanus angle maximization for catadioptric sensors with paraboloidal mirrors

Stathis Hadjidemetriou

**Dioptric cameras with conventional perspective projection have well established analytical properties. However, they suffer from perspective distortions and only have a limited field of view. Catadioptric cameras offer panoramic imaging. Their extensive field of view together with projection specific image analysis, can simplify many computer vision tasks. Several properties of catadioptric projection for geometric primitives such as points and lines have been addressed and have also been used for calibration. However, higher order geometric properties are yet to be investigated. Such analysis is complicated by the specifics of the warping of the scene by catadioptric projection. One such property, that is the subject of this work, is the Regiomontanus angle maximization relative to the effective viewpoint of the sensor. This work considers catadioptric sensors with paraboloidal mirrors, that is, paracatadioptric sensors. Analytical ray tracing of a simplified 1D world object gives its projection in the image and an expression for its length. The optimization of the length of the projection results in a third degree equation for the Regiomontanus distance that can be solved explicitly. The Khayyam geometric solution of this equation provides the Regiomontanus distance of maximum subtended projection for these cameras. Applications of these results in various contexts are presented and discussed.**

Catadioptric cameras enable panoramic imaging and offer several advantages compared to conventional cameras based on perspective projection. Panoramic imaging also provides extensive information about the environment. The benefits of catadioptric imaging together with projection specific analysis can simplify many computer vision tasks. For example, it decreases artifacts from boundary effects in image analysis and simplifies the tracking of motion. Catadioptric cameras can more closely preserve the local shape of objects. Systems based on catadioptric cameras can also enable effective visualization and even telepresence[1]. Other more recent applications are for assisted vehicle driving[2] and as robotic vision systems[3,4].

The optical properties of reflective surfaces, mirrors, namely catoptrics, were investigated geometrically since antiquity. They were initially physically associated with burning. They examined mirrors that were shaped as conic sections. The first to discover that the ellipse, the hyperbola, and the parabola are conic sections was Menaechmus (born c.380 BC). Archimedes (287-c.212 BC) worked on both conic sections and catoptrics. Apollonius of Perga (240 BC-c.190 BC) in his books "Conic sections" and "On the burning mirrors" derived the focal and reflection properties of ellipses and hyperbolas[5,6]. Diocles (240 BC-c.180 BC) in his book "On burning mirrors" derived the focal property of the parabola[7]. Later, Anthemius of Tralles (474 AC–c534 AC) wrote a book, "On burning mirrors", where he elaborated further on the properties of the foci of the parabola and of the ellipse as well as on their applicability to architecture[8]. Ptolemy (150 AD) posed the problem of reflection on a spherical surface that does not have a single viewpoint[9]. Alhazen (c.965–c.1040) in the "Book of optics" provided a geometrical solution to this problem.

In a large scale the reflective properties of the paraboloid are used for the focusing of parallel beams. Some examples are satellite dish antennas[10] and catadioptric telescopes that avoid the chromatic aberrations from which the lenses suffer[9]. Omnidirectional sensors are also used in a smaller scale for various purposes. In medicine, the ellipsoid is used for lithotripsy with ultrasound[11]. In medical imaging they have been used for endoscopy. An example has been with a cylindrical camera that gives a flat cylindrical image[12] and another example is for a system that combines forward dioptric and radial catadioptric views[13]. An early omnidirectional camera was implemented with a four-sided mirrored pyramid[14]. Also, an early system with a dodehahedral mirror enabled visualization with a single viewpoint[15]. A hyperboloid mirror has also been used for panoramic television[16]. Similarly, a catadioptric projector models the catadioptric imaging projection and inverts it to create a panoramic

Department of Information Technologies, University of Limassol, 3-5 Chaidariou Street, 3020 Limassol, Cyprus. email: stathis@uol.ac.cy

projection[17]. Also, a system for telepresence has used a hyperboloidal mirror camera[1]. More recently, omnidirectional sensors have been used for surveillance of traffic light intersections[18] as well as for assisted vehicle driving[2] and mobile robotic navigation[19]. Other uses have been as catadioptric stereo imaging sensors for mobile robotics[3,4] and as omnidirectional sensors for aerial robotics[20].

There has also been progress with analytical work on the focal properties of reflective mirror surfaces. It has been proven that any surface with a focal property both is and has to be a surface of revolution of a conic section. A proof of this result has used differential equations in polar and spherical coordinates[21]. Another proof of this result has been coordinate free based on the orthogonality properties of the foci[22]. Results along these lines were also derived and introduced to the context of computer vision by a classification of panoramic catadioptric imaging cameras with a single viewpoint constraint[23,24]. These derivations also describe the principles for the design of a catadioptric camera with a paraboloidal convex reflective surface and a quantification of its properties with respect to field of view, resolution, and blurring[23,25,26]. There have also been studies to construct an analytical model of the catadioptric projections from mirrors of different types of conic sections in a unified manner[27] and further refinements of that construction[28].

There has been extensive work on the calibration for catadioptric cameras in particular with a single viewpoint. This has been for paracatadioptric camera sensors[29] and more generally for their calibration using images of geometric primitives such as of three parallel lines[30], vanishing points[31,32], or of circular sections[33,34]. The imaging of motion has also been investigated. A study has examined the time-to-contact with paracatadioptric sensors[35]. There have also been studies on the egomotion of catadioptric sensors. A simple approach first reconstructs the motion field from the 2D image to the surface of a sphere and then applies conventional methods to estimate translation and rotation[36,37]. Other methods process directly the image of the catadioptric projection and assume correspondence to compute the essential matrix[38]. Catadioptric stereo has been achieved with various arrangements of these sensors[39–41]. The corresponding models of projection from the world to the images and the respective epipolar geometries have been developed for each of these arrangements[42].

The properties of catadioptric projection have been investigated for basic geometric primitives of points and parallel lines[31,32], simple motions of translations and rotations, as well as early computer vision operations such as calibration and stereo. The properties of the projection of many higher order geometric features of the scene have yet to be studied. This work examines one such property. This is the maximum size of the final angle an 1D object subtends in the catadioptric image projection as a function of the distance of the object. The problem has been formulated for central projection and is known as the Regiomontanus angle maximization problem. It was posed by mathematician Johannes Mueller (1436–1476)[43–45]. This work extends the Regiomontanus angle maximization for angles of a 1D object to the case where the effective viewpoint is that of a catadioptric paraboloidal imaging sensor. It examines directly the properties of the projection in catadioptric image space.

The paraboloidal mirror shape is associated with an orthographic projection. This is called a paracatadioptric imaging sensor and implements panoramic imaging with a single viewpoint. The first step is the analytical ray tracing from a point in the world, to the intermediate mirror surface, and eventually to its vertical reflection that is recorded by the camera to form an image. Then, two points in the world are considered together that are the boundaries of a 1D world object parallel to the optical axis. The distance between the orthographic projections of these two points in the image give the length of the object in the image. This length is computed and represents the angle between the parallel rays. The optimization of the length of the projection of an object results in a third degree equation for the Regiomontanus distance. This equation can be solved explicitly. The Khayyam geometric solution of this equation provides the paracatadioptric Regiomontanus distance of the object. Applications of these results for the calibration of a paracatadioptric imaging sensor, for navigation with such an imaging sensor, and a general biomedical application are discussed.

## Background

This section provides general information on paracatadioptric sensors and a formulation for Regiomontanus maximization. It also describes a catadioptric sensor with a planar mirror.

### Paracatadioptric imaging sensors

The mirror surface of a catadioptric omnidirectional sensor that has a single viewpoint has to be a surface of revolution of a conic section[21,23]. In this study the conic section giving the mirror is shaped as a paraboloid with the external surface convex and reflective. The reflected rays project to an orthographic telecentric lens in the camera that constrains the image projection to be orthographic and parallel to the optical axis. The parallel rays are assumed to meet at infinity under a negligible angle[23]. This negligible angle when measured in radians can be represented by the arc length it subtends, which is the distance between the parallel rays on the image plane. Hence, the angle difference in radians between the parallel rays is their distance on the image plane.

### Regiomontanus' angle maximization problem

It involves the angle subtended at a viewpoint directly by a 1D object that is vertical as the viewpoint moves away from the object horizontally. The coordinates in 3D space are $(x, y, z)$. This analytical development represents the $2D$ plane, $(x, y)$, with a radial coordinate $r = \frac{(x,y)}{\|(x,y)\|_2}$. The lower point of the vertical 1D object is at height $a$ and the higher point is at height $b$. The values of $z = a$ and $z = b$ satisfy $b \geq a$.

The point $a$ at distance $r$ subtends an angle $\alpha$. Similarly, the point $b$, at the same distance $r$, subtends an angle $\beta$. The subtended angle of the difference $\beta - \alpha$ as a function of $r$ is given by[43,44]:

$$\tan(\beta - \alpha) = (b - a)\frac{r}{r^2 + ab}. \tag{1}$$

The geometry is in Fig. 1a. The simulation of Eq. (1) for $(a, b) = (6, 12)$ and $r = [0, 90]$ is in Fig. 2. The maximization of the subtended angle in Eq. (1) gives the condition for radial Regiomontanus distance, $r_{RM}$. The condition can also be expressed in terms of $\tan\alpha = \frac{a}{r}$ and $\tan\beta = \frac{b}{r}$ to give

$$r_{RM} = \sqrt{ab} \Leftrightarrow \tan\alpha \tan\beta = 1 \tag{2}$$

in trigonometric form.

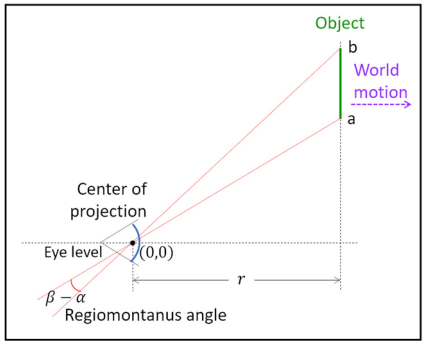


(a) Regiomontanus projection

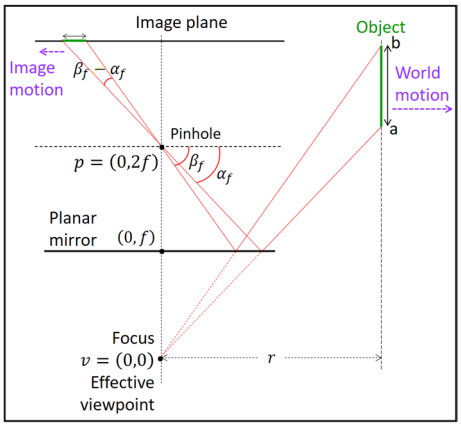


(b) Planar catadioptric projection

**Figure 1.** In (**a**) is a diagram with the geometry for direct Regiomontanus maximization. In (**b**) is a diagram with the geometry of catadioptric imaging with a planar mirror for Regiomontanus maximization.

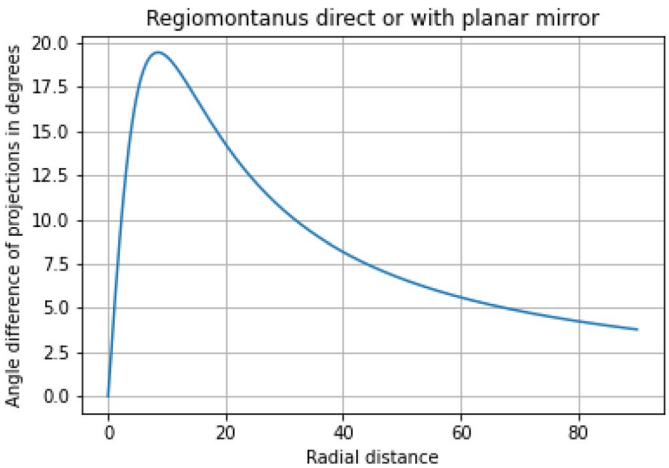


**Figure 2.** Simulation for the geometries in Fig. 1 of subtended angle $(\beta - \alpha)$ as a function of distance $r$ from an object. The values of the parameters are $(a, b) = (6, 12)$, and $r = [0, 90]$.

### Angle maximization for a planar mirror catadioptric camera

A camera is placed facing down with its center of projection, its pinhole, at a distance $f$ above a planar mirror[27]. The plane of the mirror is given by $z = f$ and the camera pinhole is taken to be at $(0, 2f)$. The result is that the effective single viewpoint is at the origin, $(0, 0)$. Hence it follows the direct Regiomontanus analysis and satisfies its results already obtained in Sect. "Regiomontanus' angle maximization problem" above. The catadioptric camera is in an upright position imaging a 1D object. In this case the difference between the final values of the projection angles optimized becomes $\beta_f - \alpha_f$.

The 1D object is parallel to the optical axis with a lower point at height $a$ and a higher point at height $b$. The trajectory of the object is normal to the optical axis. The 1D object and its trajectory, the rays emanating from the object that are reflected by the mirror impinging normally on the image, and the optical axis are all coplanar. The geometry is in the diagram in Fig. 1b. Due to the symmetry with respect to the mirror, Eq. (1) and its simulation in Fig. 2 still hold. The field of view of this catadioptric system with a planar mirror is limited. This work examines the use of a paraboloidal mirror that has an extended omnidirectional field of view and also preserves the single viewpoint constraint.

## Methods

The geometry of a vertical catadioptric camera with a planar mirror imaging a 1D object is also used for the paracatadioptric camera considered. Rays from points of the object in the world are traced analytically to the intermediate mirror surface and are then projected to the camera to form an image. The ray tracing for two points of the object, the lower and the upper, gives the projection and length of the object in the image. The derivative of the length of the projection with distance $r$ between the optical axis of the camera and the 1D object in the world is computed. Setting this derivative to zero gives a third degree equation for the Regiomontanus distance of maximum projection length.

### Paraboloidal catadioptric mirror

The axis of the paraboloid coincides with the vertical $z$-axis and its focal point is at the origin $(0, 0)$. It is also concave down, that is, $\left.\frac{d^2z}{dr^2}\right|_{r=0} < 0$. These properties are set Without Loss Of Generality (WLOG). The resulting paraboloid has equation:

$$z = f - \frac{1}{4f}r^2, \tag{3}$$

which satisfies these properties. The paraboloid intersects the $r$ axis at $(\pm 2f, 0)$ and the $z$-axis at $(0, f)$. The geometry is in Fig. 3.

### Intermediate projection on the paraboloidal mirror

The point at height $a$ and distance $r$ in the world subtends an angle $\alpha$ at the effective viewpoint. The ray emanating from the point at $a$ meets the paraboloidal mirror at $(r_{p_\alpha}, z_{p_\alpha})$ under angle:

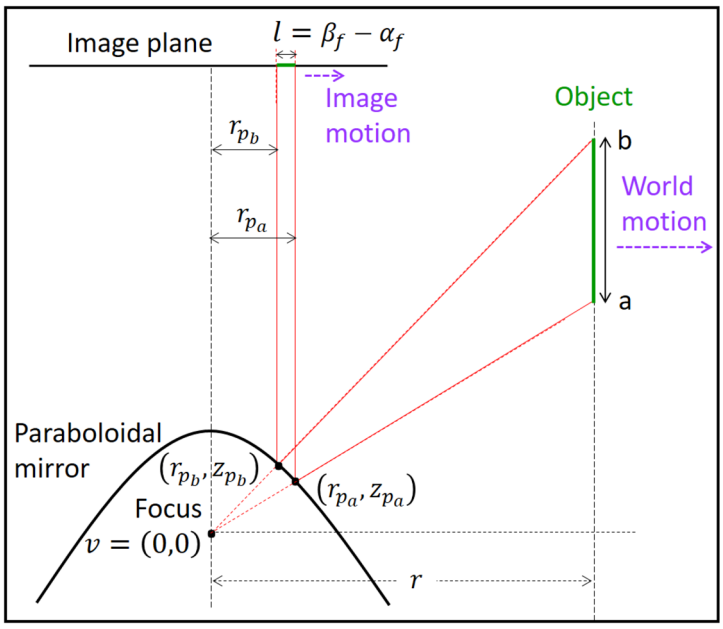


**Figure 3.** Diagram with the geometry of catadioptric imaging with a paraboloidal mirror for Regiomontanus maximization.

$$\tan\alpha = \frac{a}{r} = \frac{z_{p_\alpha}}{r_{p_\alpha}} \Rightarrow z_{p_\alpha} = r_{p_\alpha}\tan\alpha. \tag{4}$$

The replacement of Eq. (4) in Eq. (3) of the paraboloid gives:

$$r_{p_\alpha}\tan\alpha = f - \frac{1}{4f}r_{p_\alpha}^2 \Rightarrow \frac{1}{4f}r_{p_\alpha}^2 + \tan\alpha r_{p_\alpha} - f = 0. \tag{5}$$

The solution of Eq. (5) for $r_{p_\alpha}$ gives:

$$r_{p_\alpha} = 2f\left(-\tan\alpha \overset{root}{\pm} \sqrt{\tan^2\alpha + 1}\right) = 2f\left(-\tan\alpha \overset{root}{\pm} \frac{1}{\cos\alpha}\right). \tag{6}$$

The root signs of Eq. (6) correspond to the two antipodal meeting points of the ray with the mirror surface. The positive sign corresponds to the meeting point proximal to the emanating point and the negative sign corresponds to the distal meeting point. The distal point does not satisfy physical constraints and is ignored. The positive sign that corresponds to the proximal point is selected to give:

$$r_{p_\alpha} = 2f\left(-\tan\alpha + \frac{1}{\cos\alpha}\right), \tag{7}$$

with $r_{p_\alpha} > 0$. The replacement of $\tan\alpha = \frac{a}{r}$ and $\cos\alpha = \frac{r}{\sqrt{a^2+r^2}}$ in this equation gives:

$$r_{p_\alpha} = 2f\left(\frac{-a + \sqrt{a^2+r^2}}{r}\right). \tag{8}$$

## Orthographic projection for the image

The point where the ray meets the surface of the paraboloidal mirror is $(r_{p_a}, z_{p_a})$. The final projection from the mirror to the camera is orthographic. Thus, the depth coordinate, $z_{p_a}$, is ignored and the radial coordinate remains the only coordinate of interest. The radial coordinate of the projection at the mirror is the same as the radial coordinate of the projection to the camera given by Eq. (8). The derivative of the radial coordinate of the point on the mirror in Eq. (8) with respect to $r$ in space is:

$$\frac{dr_{p_\alpha}}{dr} = 2f\frac{r^2(a^2+r^2)^{-1/2} + a - (a^2+r^2)^{1/2}}{r^2}. \tag{9}$$

## Length of projection of object on the image

The image projections of the two points at heights $a$ and $b$ give the length of the 1D object in the image. The points at the surface of the paraboloidal mirror are $(r_{p_a}, z_{p_a})$ and $(r_{p_b}, z_{p_b})$. Similarly to the radial projection of point at height $a$ under angle $\alpha$ in Eq. (8), the point at height $b$ and under angle $\beta$ has radial projection $r_{p_\beta}$. The rays projecting on the image plane are parallel. Hence the difference between the final values of the angles, $\beta_f - \alpha_f$, in radians, is equal to the length of the projection, $l$. The length of the projection in the image is the difference between the $r$-coordinates of the projections of points $a$ and $b$ in the image, $l = r_{p_\alpha} - r_{p_\beta}$,

$$l = r_{p_\alpha} - r_{p_\beta} = 2f\left(\frac{-a + \sqrt{a^2+r^2}}{r}\right) - 2f\left(\frac{-b + \sqrt{b^2+r^2}}{r}\right). \tag{10}$$

Equations (9) and (10) give the derivative of the length of the projection as:

$$\begin{aligned}\frac{dl}{dr} &= \frac{d(r_{p_\alpha} - r_{p_\beta})}{dr} = \frac{dr_{p_\alpha}}{dr} - \frac{dr_{p_\beta}}{dr} \\ &= 2f\left[\frac{r^2(a^2+r^2)^{-1/2} + a - (a^2+r^2)^{1/2}}{r^2}\right] - \\ &\quad -2f\left[\frac{r^2(b^2+r^2)^{-1/2} + b - (b^2+r^2)^{1/2}}{r^2}\right].\end{aligned} \tag{11}$$

## Maximization of the length of the projection of the object in the image

The condition for the maximum is $\frac{dl(r)}{dr} = 0$. Considering Eq. (11), this leads to,

$$\begin{aligned}2f\left[\frac{r^2(a^2+r^2)^{-1/2} + a - (a^2+r^2)^{1/2}}{r^2}\right] - 2f\left[\frac{r^2(b^2+r^2)^{-1/2} + b - (b^2+r^2)^{1/2}}{r^2}\right] &= 0 \\ \Rightarrow \\ r^2\left[(a^2+r^2)^{-1/2} - (b^2+r^2)^{-1/2}\right] + (a-b) - \left[(a^2+r^2)^{1/2} - (b^2+r^2)^{1/2}\right] &= 0.\end{aligned} \tag{12}$$

The rationalization of the denominators in Eq. (12) is developed in appendix A of supplementary information to give the maximization condition as:

$$b^2(a^2+r^2)^{1/2} - a^2(b^2+r^2)^{1/2} - (b-a)(a^2+r^2)^{1/2}(b^2+r^2)^{1/2} = 0. \tag{13}$$

This equation is simplified with the removal of the radicals. The development is in appendix B of supplementary information. It gives an intermediate polynomial of eighth degree in the powers of $r$, $\sum_{i=0}^{8} c_i'(a,b)r^i = 0$. The polynomial is even in terms of the powers of $r$ and the zeroth order term is zero. The odd terms are zero because of the symmetry of the problem around the axis $x = 0$ . The zeroth order term is zero because both the projection and its derivative are zero at $x = 0$.

The coefficients of the powers of $r$ of the eighth degree polynomial are in turn polynomials of $a$ and $b$. The coefficients are simplified by removing terms that are common to all of them. The result is an equation of the form:

$$r^2\left(c_8(a,b)r^6 + c_6(a,b)r^4 + c_4(a,b)r^2 + c_2(a,b)\right) = 0, \tag{14}$$

where $c_8(a,b)$, $c_6(a,b)$, $c_4(a,b)$, and $c_2(a,b)$ are polynomials of powers of $a$ and $b$ as computed in appendix B of supplementary information and given in Table 1. The symbolic algebraic development of the methodologies in appendix B of supplementary information and of this work in general make use of the SymPy software library[46] of the Python programming language[47].

The condition in Eqs. (13) and (14) has at least a double root at $r = 0$; however, as Eq. (10) can show, this corresponds to an object projection of length $lim_{r\to 0} l = 0$. Also, the configuration with the camera located immediately above the mirror renders the solution for $r = 0$ physically impossible. Hence, this solution is ignored.

The polynomial from Eq. (14) that remains is:

$$c_8(a,b)r^6 + c_6(a,b)r^4 + c_4(a,b)r^2 + c_2(a,b) = 0. \tag{15}$$

The replacement:

$$w = r^2 \tag{16}$$

gives:

$$c_8(a,b)w^3 + c_6(a,b)w^2 + c_4(a,b)w + c_2(a,b) = 0 \tag{17}$$

The development of the solution of this equation is in Sect. "Geometric solution of the cubic polynomial equation" below.

## Geometric solution of the cubic polynomial equation

Equation (17) is a third degree equation. The constrain $w = r^2 > 0$ gives real final solutions for the Regiomontanus distance as $r = \sqrt{w}$ in Eq. (16). The algebraic solution to the cubic equations can be computed directly with the method of Cardano[48]. However, that method is inconvenient. Instead, this section presents a more intuitive geometric solution of this equation provided by Omar Khayyam that conveniently provides their roots[48]. The solutions for $w$ are described as intersections of conic sections. Specifically, the intersection of a parabola and hyperbola. The solution steps are given below.

### *Depressed form of cubic equation*

A polynomial in standard form in Eq. (17) is normalized so that the coefficient of the third order becomes unity to give:

$$w^3 + \frac{c_6}{c_8}w^2 + \frac{c_4}{c_8}w + \frac{c_2}{c_8} = 0 \tag{18}$$

The substitutions for the fractions:

$$c_p = \frac{c_6}{c_8}, \quad c_g = \frac{c_4}{c_8}, \quad c_r = \frac{c_2}{c_8} \tag{19}$$

in Eq. (18) give:

| Eighth degree polynomial coefficients | Expressions of $a$ and $b$ |
|---|---|
| $c_8(a,b)$ | $(b-a)^2$ |
| $c_6(a,b)$ | $-4ab(a^2-ab+b^2)$ |
| $c_4(a,b)$ | $4a^2b^2(a^2-ab+b^2)$ |
| $c_2(a,b)$ | $4a^4b^4$ |

**Table 1.** The coefficients of the eighth degree polynomial directly in terms of $a$ and $b$.

$$w^3 + c_p w^2 + c_g w + c_r = 0. \tag{20}$$

A cubic is symmetric around its inflection point. The inflection point of Eq. (20) is located at $w = -\frac{c_p}{3}$. The cubic is shifted so that the inflection point is located on the vertical axis. This gives its depressed form where the quadratic term is zero. This is achieved with the substitution,

$$\chi = w + \frac{c_p}{3} \Rightarrow w = \chi - \frac{c_p}{3} \tag{21}$$

in Eq. (20) to give Eq. (22) and finally Eq. (23):

$$\left(\chi - \frac{c_p}{3}\right)^3 + c_p\left(\chi - \frac{c_p}{3}\right)^2 + c_g\left(\chi - \frac{c_p}{3}\right) + c_r = 0 \Rightarrow \tag{22}$$

$$\begin{aligned}
\left(\chi - \frac{c_p}{3}\right)^2\left(\chi - \frac{c_p}{3} + c_p\right) + c_g\left(\chi - \frac{c_p}{3}\right) + c_r &= 0 \Rightarrow \\
\left(\chi - \frac{c_p}{3}\right)^2\left(\chi + \frac{2c_p}{3}\right) + c_g\left(\chi - \frac{c_p}{3}\right) + c_r &= 0 \Rightarrow \\
\left(\chi - \frac{c_p}{3}\right)\left[\left(\chi - \frac{c_p}{3}\right)\left(\chi + \frac{2c_p}{3}\right) + c_g\right] + c_r &= 0 \Rightarrow \\
\left(\chi - \frac{c_p}{3}\right)\left[\chi^2 + \frac{c_p}{3}\chi - \frac{2}{9}c_p^2 + c_g\right] + c_r &= 0 \Rightarrow \\
\chi^3 + \frac{c_p}{3}\chi^2 - \frac{2}{9}c_p^2\chi + c_g\chi - \frac{c_p}{3}\chi^2 - \frac{c_p^2}{9}\chi + \frac{2}{27}c_p^3 - \frac{c_p}{3}c_g + c_r &= 0 \Rightarrow \\
\chi^3 + \chi\left(c_g - \frac{c_p^2}{3}\right) + \left(\frac{2}{27}c_p^3 - \frac{c_p}{3}c_g + c_r\right) &= 0
\end{aligned} \tag{23}$$

The substitutions of the coefficient of $\chi$ in Eq. (23) with $c_s$ and the zero order term in the same equation with $c_t$ gives:

$$c_s = c_g - \frac{c_p^2}{3}, \quad c_t = \frac{2}{27}c_p^3 - \frac{c_p}{3}c_g + c_r. \tag{24}$$

The substitution of the relations in Eq. (24) above into Eq. (23) gives:

$$\chi^3 + c_s\chi + c_t = 0. \tag{25}$$

The substitutions of $c_g$, $c_p$, and $c_r$ from Eq. (19) in Eq. (24) gives both $c_s$ and $c_t$ as a function of $c_2$, $c_4$, $c_6$, and $c_8$. The $c_s$ becomes

$$c_s = c_g - \frac{c_p^2}{3} = \frac{c_4}{c_8} - \frac{1}{3}\frac{c_6^2}{c_8^2} = \frac{3c_4c_8 - c_6^2}{3c_8^2} \tag{26}$$

and the $c_t$ becomes:

$$\begin{aligned}
c_t &= \frac{2}{27}c_p^3 - \frac{c_p}{3}c_g + c_r = \frac{2}{27}\frac{c_6^3}{c_8^3} - \frac{c_6}{3c_8}\frac{c_4}{c_8} + \frac{c_2}{c_8} = \\
&= \frac{2c_6^3 - 9c_4c_6c_8 + 27c_8^2c_2}{27c_8^3}.
\end{aligned} \tag{27}$$

The substitutions of $c_2$, $c_4$, $c_6$, $c_8$ from Table 1 in Eqs. (26) and (27), respectively, give

$$c_s = -\frac{4a^2b^2\left(a^4 + a^3b + ab^3 + b^4\right)}{3a^4 - 12a^3b + 18a^2b^2 - 12ab^3 + 3b^4} \tag{28}$$

and

$$c_t = \frac{4a^3b^3\left(4a^6 - 21a^5b - 12a^4b^2 + 26a^3b^3 - 12a^2b^4 - 21ab^5 + 4b^6\right)}{27\left(a^6 - 6a^5b + 15a^4b^2 - 20a^3b^3 + 15a^2b^4 - 6ab^5 + b^6\right)}. \tag{29}$$

The coefficients of the depressed polynomial in terms of $a$ and $b$ are also given in Table 2.

These relations can more conveniently be expressed in terms of $\frac{b}{a}$ to give:

| Depressed polynomial coefficients | Expressions of $a$ and $b$ |
|---|---|
| $c_s$ | $-\frac{4a^2b^2(a^4+a^3b+ab^3+b^4)}{3a^4-12a^3b+18a^2b^2-12ab^3+3b^4}$ |
| $c_t$ | $\frac{4a^3b^3(4a^6-21a^5b-12a^4b^2+26a^3b^3-12a^2b^4-21ab^5+4b^6)}{27(a^6-6a^5b+15a^4b^2-20a^3b^3+15a^2b^4-6ab^5+b^6)}$ |

**Table 2.** The coefficients of the depressed polynomial directly in terms of $a$ and $b$.

$$c_s = -\frac{4}{3}a^2b^2\frac{\left(1+\left(\frac{b}{a}\right)+\left(\frac{b}{a}\right)^3+\left(\frac{b}{a}\right)^4\right)}{\left(1-4\left(\frac{b}{a}\right)+6\left(\frac{b}{a}\right)^2-4\left(\frac{b}{a}\right)^3+\left(\frac{b}{a}\right)^4\right)} \tag{30}$$

and

$$c_t = \frac{4}{27}a^3b^3\frac{\left(4-21\left(\frac{b}{a}\right)-12\left(\frac{b}{a}\right)^2+26\left(\frac{b}{a}\right)^3-12\left(\frac{b}{a}\right)^4-21\left(\frac{b}{a}\right)^5+4\left(\frac{b}{a}\right)^6\right)}{\left(1-6\left(\frac{b}{a}\right)+15\left(\frac{b}{a}\right)^2-20\left(\frac{b}{a}\right)^3+15\left(\frac{b}{a}\right)^4-6\left(\frac{b}{a}\right)^5+\left(\frac{b}{a}\right)^6\right)}. \tag{31}$$

The denominator of the fraction in Eq. (30) for $c_s$ is equal to zero for $\frac{b}{a}=1$ and positive for $\frac{b}{a}>1$. Hence, when $\frac{b}{a}>1$, that is the range of interest, then $c_s<0$. The value of $c_t$ in Eq. (31) can be both positive and negative in the range of interest, $\frac{b}{a}>1$.

*Khayyam's geometric solutions*

The cubic equations can be classified into several Khayyam types so that the coefficients are positive. Each type is solved differently. Several of the types are either reducible to simpler ones or do not result in real solutions[48]. The two remaining types that are relevant in this work are in Table 3. In the range of interest, $\frac{b}{a}>1$, the coefficient $c_s$ satisfies $c_s<0$ and the coefficient $c_t$ satisfies $c_t<0$ and $c_t>0$. Hence, Eq. (25) can be of type 3 or of type 2 and the geometric solutions for these two types are given below.

*Khayyam's solutions for type 3 and type 2*

The Khayyam equation of type 3 is:

$$\chi^3 = c_{3,a}\chi + c_{3,b}. \tag{32}$$

Its geometric solution is in Fig. 4a. The Khayyam equation of type 2 is:

$$\chi^3 + c_{2,b} = c_{2,a}\chi. \tag{33}$$

Its geometric solution is in Fig. 4a.

Khayyam treated these types in Eq. (32) and in Eq. (33) separately but by allowing negative horizontal lengths we can combine these two types and corresponding solutions into one:

$$\chi^3 \pm c_{23,b} = c_{23,a}\chi. \tag{34}$$

Let $AB$ be perpendicular to $BC$. Two auxiliary shapes are employed. The first is a square with side $AB$ so that:

$$(AB)^2 = c_{23,a}. \tag{35}$$

The second auxiliary shape is a solid with base equal to $(AB)^2$ and volume equal to $c_{23,b}$:

$$(AB)^2 \cdot BC = c_{23,b}. \tag{36}$$

Place $BC$ to the left if the sign in front of $c_{23,b}$ is negative (Type 3) as in Fig. 4a. Place $BC$ to the right if the sign in front of $c_{23,b}$ is positive (Type 2) as in Fig. 4b. The first main shape is a parabola with vertex at $B$ and parameter $AB$. The definition and equation of the parabola with $(BE)=\chi$ and $(BZ)=y$ becomes:

| $c_s c_t$ | Assignments | Type |
|---|---|---|
| $c_s<0 c_t<0$ | $c_{3,a}=-c_s c_{3,b}=-c_t$ | Type 3 |
| $c_s<0 c_t>0$ | $c_{2,a}=-c_s c_{2,b}=c_t$ | Type 2 |

**Table 3.** The two types of equations for solutions.

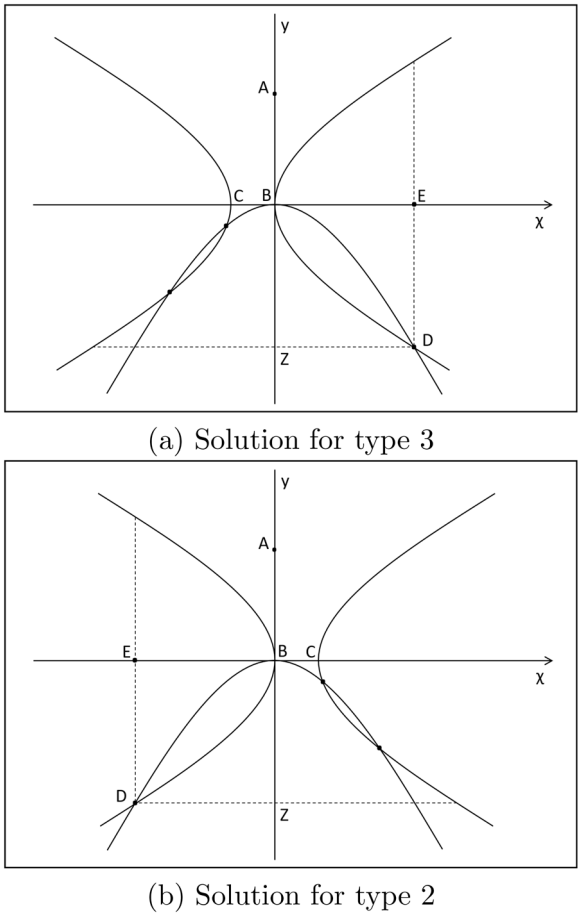


**Figure 4.** In (**a**) is the solution for type 3 and in (**b**) is the solution for type 2.

$$(BE)^2 = (BZ)(AB) \Rightarrow \chi^2 = y\sqrt{c_{23,a}} \Rightarrow y = \frac{\chi^2}{\sqrt{c_{23,a}}}. \tag{37}$$

The square of Eq. (37),

$$y^2 = \frac{\chi^4}{c_{23,a}}, \tag{38}$$

is also used for convenience. The replacement of $c_{23,a}$ in Eq. (37) gives the parabola as

$$y = \sqrt{\frac{3a^4 - 12a^3b + 18a^2b^2 - 12ab^3 + 3b^4}{4a^2b^2\left(a^4 + a^3b + ab^3 + b^4\right)}}\chi^2. \tag{39}$$

The second main shape is a hyperbola with vertices $B$ and $C$ and parameter $BC$ as is shown in Fig. 4. The definition and equation of the hyperbola is:

$$(ED)^2 = (BE)(CE) \tag{40}$$

It involves the length of $BC$ given by replacing Eq. (35) in Eq. (36) to get:

$$(AB)^2(BC) = c_{23,b} \Rightarrow c_{23,a}(BC) = c_{23,b} \Rightarrow (BC) = \frac{c_{23,b}}{c_{23,a}}. \tag{41}$$

*Khayyam's solutions for Type 3*
In type 3 the definition of the hyperbola leads to:

$$(BE) = \chi \Rightarrow (CE) = (EB) + (BC) = \chi + \frac{c_{3,b}}{c_{3,a}} \tag{42}$$

The definition and equation of hyperbola in Eq. (40) for relation (42) of type 3 is

$$(ED)^2 = (BE)(CE) \Rightarrow y^2 = \chi\left(\chi + \frac{c_{3,b}}{c_{3,a}}\right) \Rightarrow y^2 = \chi^2 + \frac{c_{3,b}}{c_{3,a}}\chi. \tag{43}$$

The parameter of this equation is $\frac{c_{3,b}}{c_{3,a}} = \frac{c_t}{c_s}$.

The meeting point $D$ of the parabola and hyperbola with $\chi = (BE)$ and $y = (ED)$ is a solution. Substitute to Eq. (43) of the hyperbola above the relation $y^2 = \frac{\chi^4}{c_{3,a}}$ of the square of the equation of the parabola from Eq. (38) to get:

$$y^2 = \chi^2 + \frac{c_{3,b}}{c_{3,a}}\chi \Rightarrow \frac{\chi^4}{c_{3,a}} = \chi^2 + \frac{c_{3,b}}{c_{3,a}}\chi \Rightarrow \chi^3 = c_{3,a}\chi + c_{3,b} \tag{44}$$

This is indeed type 3 of Khayyam's in equation (32).

*Khayyam's solutions for type 2*

In type 2 the definition of the hyperbola leads to:

$$(BE) = -\chi \Rightarrow (CE) = (BE) + (BC) \Rightarrow (CE) = -\chi + \frac{c_{2,b}}{c_{2,a}} \tag{45}$$

The definition and equation of hyperbola in Eq. (40) for relation (45) of type 2 is

$$(ED)^2 = (BE)(CE) \Rightarrow y^2 = -\chi\left(-\chi + \frac{c_{2,b}}{c_{2,a}}\right) \Rightarrow y^2 = \chi^2 - \frac{c_{2,b}}{c_{2,a}}\chi \tag{46}$$

The parameter of this equation is $-\frac{c_{2,b}}{c_{2,a}} = \frac{c_t}{c_s}$.

The meeting point $D$ of the parabola and hyperbola with $\chi = (BE)$ and $y = (ED)$ is a solution. Substitute to Eq. (46) above of the hyperbola the relation $y^2 = \frac{\chi^4}{c_{2,a}}$ of the square of the equation of the parabola from Eq. (38) to get:

$$y^2 = \chi^2 - \frac{c_{2,b}}{c_{2,a}}\chi \Rightarrow \frac{\chi^4}{c_{2,a}} - \chi^2 + \frac{c_{2,b}}{c_{2,a}}\chi = 0 \Rightarrow \chi^3 + c_{2,b} = c_{2,a}\chi. \tag{47}$$

This is indeed type 2 of Khayyam's in equation (33).

*Khayyam's solutions for type 3 and type 2 at intersections of hyperbola and parabola*

The equation of the hyperbola both on type 3 in Eq. (43) and type 2 in Eq. (46) by replacing the coefficients becomes:

$$\begin{aligned} y^2 =& \chi^2 + \frac{ab\left(-4a^4 + 29a^3b - 42a^2b^2 + 29ab^3 - 4b^4\right)}{9\left(a^4 - 3a^3b + 4a^2b^2 - 3ab^3 + b^4\right)}\chi \\ =& \chi^2 + \frac{ab\left(-4 + 29\left(\frac{b}{a}\right) - 42\left(\frac{b}{a}\right)^2 + 29\left(\frac{b}{a}\right)^3 - 4\left(\frac{b}{a}\right)^4\right)}{9\left(1 - 3\left(\frac{b}{a}\right) + 4\left(\frac{b}{a}\right)^2 - 3\left(\frac{b}{a}\right)^3 + \left(\frac{b}{a}\right)^4\right)}\chi. \end{aligned} \tag{48}$$

Each intersection of parabola in Eq. (39) and hyperbola in Eq. (48), except of $B$ at the origin, gives a root of the cubic[48].

*Recovery of roots of original polynomial*

The Khayyam's solution are for the depressed form of the cubic in Eq. (25). The solutions for the standard form of the cubic in Eq. (18) are recovered using the relation in Eq. (21) with:

$$w = \chi - \frac{c_p}{3} > 0. \tag{49}$$

The value of $c_p$ as a function of $a$ and $b$ is obtained from Eq. (19) and Table 1:

$$c_p = \frac{c_6}{c_8} = \frac{-4ab(a^2 - ab + b^2)}{(b-a)^2} = -4ab\left(1 + \frac{ab}{(b-a)^2}\right). \tag{50}$$

This expression for $c_p$ in terms of $a$ and $b$ shows that $c_p < 0$. Hence, the term $-\frac{c_p}{3} \geq 0$, in relation (49) is able to map a negative value of $\chi$ into a positive value of $w$.

The value of $w$ must be greater than zero. This is because from Eq. (16) the square root of $w$ gives the value of $r$,

$$r = \pm\sqrt{w} = \pm\sqrt{\chi - \frac{c_p}{3}} = \pm\sqrt{\chi + \frac{4ab}{3}\left(1 + \frac{ab}{(b-a)^2}\right)}, \tag{51}$$

that must be a real number for a meaningful physical solution. The value of $r$ can be positive or negative due to the symmetry around the optical axis.

This shows that for type 3 it may be necessary to check one, two, or even three roots $\chi$ if they are positive. It also shows that for type 2 it may be necessary to check two or even three roots $\chi$ if they are positive. A solution must then also be checked to satisfy the original condition in Eq. (13).

## Discussion

This work develops a method to compute the Regiomontanus distance that maximizes the length of the projection of a 1D object imaged with a paracatadioptric sensor, that is, using a paraboloidal mirror. The optical axis is assumed vertical since, in practice, catadioptric omnidirectional sensors are fixed on another object such as a wall, a vehicle, a ground robot, or an aerial robot (Unmanned Aerial Vehicle). The direction of the vertical axis can be upwards or downwards depending on the application.

The first step of the methodology is to trace rays from two world points bounding a 1D object to the mirror surface. Then, the orthographic projection on the paracatadiotric camera sensor simplifies the computation of the image projection. The expression giving the length of the projection, $l$, is computed as a function of the distance between the optical axis of the sensor and the 1D object. The derivative of this expression is set to zero, $\frac{dl}{dt} = 0$, to give the maximization condition through the developments in Sect. "Length of projection of object on the image", "Maximization of the length of the projection of the object in the image", and "Geometric solution of the cubic polynomial equation". This condition is a third degree equation that can be solved directly. In this work, this equation is solved geometrically with Khayyam's method to provide in a more meaningful way the Regiomontanus distance. The solutions for the Regiomontanus distance do not depend on parameter $f$ of the paraboloid because of the orthographic projection forming the final image.

The Regiomontanus analysis can be extended to single viewpoint catadioptric sensors with hyperboloid and ellipsoid mirrors that involve a central projection from the mirror to the camera. The derivations can also be extended to more general situations for a 1D object in 3D space. In that case a linear trajectory of an object may not be co-planar with the optical axis, in which case the projection of the trajectory will be a conic section[29–32,49]. The projections of the trajectories of its two end points will be two different conic sections that meet at two vanishing points that correspond to the two opposite directions along the linear trajectories[30]. There exist methodologies for the analysis of the projection of parallel lines on catadioptric sensors to conic sections[31]. The Regiomontanus approach is complementary to those in that it investigates the effect of radial motion across such projected conic sections. The extension can also be for a general projection of a 2D object in 3D space or a 3D object.

The analysis presented in this work can have direct applications in various contexts. It can be used for teleconferencing and for online remote teaching under optimal viewing angles. Notably, the Regiomontanus angle is independent of the focal length ($f$) or on other intrinsic camera parameter, making it applicable even for uncalibrated cameras. However, the initial portion of this study, which computes the radial length of the projection, has the potential to contribute to paracatadioptric calibration. This calibration method would be simpler than existing approaches based on images of geometric primitives such as parallel lines and vanishing points[31] that require the fitting of conic sections[31,33,34]. Other applications of this Regiomontanus analysis can be for the navigation and positioning using paracatadioptric sensors such as those used by robots in indoor environments[19] as in a museum and aerial robotics in outdoor environments. These results may extend to other contexts where the focal properties of conic sections play a role, such as ultrasound-based imaging and therapies. In those contexts, the ultrasound waves under Regiomontanus angle could potentially enhance imaging resolution.

The Regiomontanus angle maximization can be derived for other types of catadioptric sensors or even under different media. The results presented in this study can be implemented and tested experimentally in various contexts.

## Data availability

The data and materials are promptly available to readers by contacting the corresponding author, Stathis Hadjidemetriou, email: stathis@uol.ac.cy.

## Code availability

The code is promptly available to readers by contacting the author.

Received: 4 August 2023; Accepted: 6 August 2024
Published online: 09 August 2024

## References

1. Onoe, Y., Yamazawa, K., Takemura, H. & Yokoya, N. Telepresence by real-time view-dependent image generation from omnidirectional video streams. *Comput. Vis. Image Underst.* **71**, 588–592 (1998).
2. Vu, A., & Barth, M. Catadioptric omnidirectional vision sensor integration for vehicle-based sensing. In *2009 12th International IEEE Conference on Intelligent Transportation Systems*, pp 1–7 (2009).
3. Lin, Shih-Schon, & Bajcsy, R. High resolution catadioptric omni-directional stereo sensor for robot vision. In *2003 IEEE International Conference on Robotics and Automation (Cat. No. 03CH37422)*, volume **2**, pp 1694–1699 (2003)
4. Benosman, R., Deforas, E., & Devars, J. A new catadioptric sensor for the panoramic vision of mobile robots. In *Proceedings IEEE Workshop on Omnidirectional Vision (Cat. No. PR00704)*, pp 112–116 (2000).
5. Heath, T. *A History of Greek Mathematics* (Oxford University Press, 1921).
6. Fried, M. N. *Edmond Halley's Reconstruction of the Lost Book of Apollonius's Conics: Translation and Commentary* (Springer, 2011).
7. Toomer, G. J. *Diocles, On Burning Mirrors: The Arabic Translation of the Lost Greek Original* (Springer, 1976).
8. Dupuy, L. *Anthemius of Tralles: On remarkable mechanical devices* (1777).
9. Gerard, R. L. *Astronomical Optics and Elasticity Theory, Active Optics Methods* (Springer, 2009).
10. Rudge, A. W. & Adatia, N. A. Offset-parabolic-reflector antennas: A review. *Proc. IEEE* **66**(12), 1592–1618 (1978).

11. Cleveland, R. O. The acoustics of shock wave lithotripsy. In *AIP Conference Proceedings*, p 900 (2007).
12. Greguss, P. The tube peeper: A new concept in endoscopy. *Opt. Laser Technol.* **17**(1), 41–45 (1985).
13. Wang, R. C. C., Deen, M. J., Armstrong, D. & Fang, Q. Development of a catadioptric endoscope objective with forward and side views. *J. Biomed. Opt.* **16**(6), 1–16 (2011).
14. Nalwa, V. S. A true omni-directional viewer. *Bell Laboratories Technical Memorandum*, BL0115500-960115-01 (1996).
15. Raskar, R., *et al.* The office of the future: A unified approach to image-based modeling and spatially immersive displays. In *ACM SIGGRAPH*, pp 179–188 (1998).
16. Rees, D. W. Panoramic television viewing system. *United States Patent*, US3505465A (1970).
17. Ding, Y., Xiao, J., Tan, K.-H., & Yu, J. Catadioptric projectors. In *2009 IEEE Conference on Computer Vision and Pattern Recognition*, pp 2528–2535 (2009).
18. Cao, M., Vu, A., & Barth, M. A novel omni-directional vision sensing technique for traffic surveillance. In *2007 IEEE Intelligent Transportation Systems Conference*, pp 678–683 (2007).
19. Vasseur, P. & Morbidi, F. *Omnidirectional Vision: From Theory to Applications* (ISTE-Wiley, Berlin, 2023).
20. Natraj, A., Ly, D. S., Eynard, D., Demonceaux, C. & Vasseur, P. Omnidirectional vision for UAV: Applications to attitude, motion and altitude estimation for day and night conditions. *J. Intel. Robot. Syst.* **69**, 459–473 (2013).
21. Drucker, D. Reflection properties of curves and surfaces. *Math. Mag.* **65**(3), 147–157 (1992).
22. Drucker, D. & Locke, P. A natural classification of curves and surfaces with reflection properties. *Math. Mag.* **69**, 249–256 (1996).
23. Baker, S. & Nayar, S. K. A theory of single-viewpoint catadioptric image formation. *Int. J. Comput. Vis.* **35**(2), 175–196 (1999).
24. Baker, S., & Nayar, S. K. A theory of catadioptric image formation. In *IEEE International Conference on Computer Vision (ICCV)*. pp 35–42 (1998).
25. Nayar, S. K. Omnidirectional video camera. In *DARPA Image Understanding Workshop (IUW)*, pp 235–242 (1997).
26. Nayar, S. K. Catadioptric omnidirectional camera. In *IEEE Conference on Computer Vision and Pattern Recognition (CVPR)*, pp 482–488 (1997).
27. Daniilidis, K., Geyer, C. Omnidirectional vision: Theory and algorithms. In *Proceedings 15th International Conference on Pattern Recognition. ICPR-2000*, volume **1**, pp 89–96 (2000).
28. Barreto, J. P., & Araujo, H. Issues on the geometry of central catadioptric image formation. In *Proceedings of the 2001 IEEE Computer Society Conference on Computer Vision and Pattern Recognition. CVPR 2001*, volume **2**, pp II–II (2001).
29. Geyer, C. & Daniilidis, K. Paracatadioptric camera calibration. *IEEE Trans. Pattern Anal. Mach. Intell.* **24**(5), 687–695 (2002).
30. Barreto, J. P. & Araujo, H. Geometric properties of central catadioptric line images and their application in calibration. *IEEE Trans. Pattern Anal. Mach. Intell.* **27**(8), 1327–1333 (2005).
31. Miraldo, P., Eiras, F., & Ramalingam, S. Analytical modeling of vanishing points and curves in catadioptric cameras. In *Proceedings of the IEEE Conference on Computer Vision and Pattern Recognition (CVPR)*, (2018).
32. Miraldo, P., & Iglesias, J. A unified model for line projections in catadioptric cameras with rotationally symmetric mirrors. In *Proceedings of the IEEE/CVF Conference on Computer Vision and Pattern Recognition (CVPR)*, pp 15797–15806 (2022).
33. Yang, R., & Zhang, J. A calibration method for paracatadioptric cameras based on circular sections. *Multimedia Tools Appl.*, (2022).
34. Yang, F., Zhao, Y. & Wang, X. Common pole-polar properties of central catadioptric sphere and line images used for camera calibration. *Int. J. Comput. Vis.* **131**, 121–133 (2023).
35. Benamar, F., Elfkihi, S., Demonceaux, C., Mouaddib, E. & Aboutajdine, D. Visual contact with catadioptric cameras. *Robot. Auton. Syst.* **64**, 100–119 (2015).
36. Gluckman, J. M., & Nayar, S. K. Ego-motion and omnidirectional cameras. In *Sixth International Conference on Computer Vision (IEEE Cat. No. 98CH36271)*, pp 999–1005 (1998).
37. Bruss, A. R. & Horn, B. K. P. Passive navigation. *Comput. Vis. Gr. Image Process.* **21**(1), 3–20 (1983).
38. Yagi, Y., Nishii, W., Yamazawa, K., & Yachida, M. Rolling motion estimation for mobile robot by using omnidirectional image sensor hyperomnivision. In *Proceedings of 13th International Conference on Pattern Recognition*, volume **1**, pp 946–950 (1996).
39. Gluckman, J. M., Nayar, S. K., & Thoresz, K. J. Real-time omnidirectional and panoramic stereo. In *DARPA Image Understanding Workshop (IUW)* 299–303 (1998).
40. Gluckman, J. M. & Nayar, S. K. Rectified catadioptric stereo sensors. In *IEEE Conference on Computer Vision and Pattern Recognition (CVPR)***2**, 380–387 (2000).
41. Gonzalez-Barbosa, J.-J., & Lacroix, S. Fast dense panoramic stereovision. In *Proceedings of the 2005 IEEE International Conference on Robotics and Automation*, pp 1210–1215 (2005).
42. Svoboda, T. & Pajdla, T. Epipolar geometry for central catadioptric cameras. *Int. J. Comput. Vis.* **49**, 23–37 (2002).
43. Dorrie, H. *100 Great Problems of Elementary Mathematics* (Dover Books on Mathematics, 1965).
44. Maor, E. *Trigonometric Delights* (Princeton University Press, 2002).
45. Stewart, J. *Calculus: Early Transcendentals* 5th edn. (Brooks/Cole, 2003).
46. Meurer, A. *et al.* Sympy: Symbolic computing in python. *PeerJ Comput. Sci.* **3**, e103 (2017).
47. Van Rossum, G. & Drake, F. L. *Python 3 Reference Manual* (CreateSpace, 2009).
48. Henderson, D. W., & Taimina, D. Experiencing geometry: In *Euclidean, spherical and hyperbolic spaces* (2nd Edition) Prentice Hall, Upper Saddle River, New Jersey, USA (2001).
49. Geyer, C., & Daniilidis, K. Catadioptric camera calibration. In *Proceedings of the Seventh IEEE International Conference on Computer Vision*, volume **1**, pp 398–404 (1999).



## Acknowledgements
I would like to thank Dr. Katerina Kaouri, Reader of applied mathematics in the school of mathematics of Cardiff University, UK, for her advice that have helped me improve this work.

## Funding
The authors declare that no funds, grants, or other support were received during the preparation of this manuscript.


## Competing interests
The authors declare no competing interests.

## Additional information
**Supplementary Information** The online version contains supplementary material available at https://doi.org/10.1038/s41598-024-69498-x.

**Correspondence** and requests for materials should be addressed to S.H.

**Reprints and permissions information** is available at www.nature.com/reprints.

**Publisher's note** Springer Nature remains neutral with regard to jurisdictional claims in published maps and institutional affiliations.

**Open Access** This article is licensed under a Creative Commons Attribution-NonCommercial-NoDerivatives 4.0 International License, which permits any non-commercial use, sharing, distribution and reproduction in any medium or format, as long as you give appropriate credit to the original author(s) and the source, provide a link to the Creative Commons licence, and indicate if you modified the licensed material. You do not have permission under this licence to share adapted material derived from this article or parts of it. The images or other third party material in this article are included in the article's Creative Commons licence, unless indicated otherwise in a credit line to the material. If material is not included in the article's Creative Commons licence and your intended use is not permitted by statutory regulation or exceeds the permitted use, you will need to obtain permission directly from the copyright holder. To view a copy of this licence, visit http://creativecommons.org/licenses/by-nc-nd/4.0/.

© The Author(s) 2024